PNAS RESEARCH ARTICLE | CHEMISTRY

Tetrathienylethene-based porous framework composites for boosting photocatalytic antibacterial activity

Si Ma[a,b,1], Yintung Lam[c,1], Le Shi[a,b], Jian Yang[a,b], Kun Wang[a,b], Bo Yu[c], Chiwai Kan[c,2], Bin Fei[c], John H. Xin[c], Kaikai Ma[c,2], J. Fraser Stoddart[a,b,d,e,f,g], and Zhijie Chen[a,b,2]

Affiliations are included on p. 7.

Edited by Peter Stang, The University of Utah, Salt Lake City, UT; received November 6, 2024; accepted March 4, 2025

In order to reduce the risk of high-threat pathogens, a photocatalytic antibacterial method with a reputation for high efficiency and sustainability has attracted widespread attention. Recently, metal-organic frameworks (MOFs) have emerged as desirable platforms for photocatalytic applications by virtue of their structural diversity and functional adjustability. Herein, we report that we have synthesized a stable and photosensitive zirconium-based MOF (Zr-MOF) with a photoactive tetrathienylethene-based organic linker, Zr-TSS-1. Compared with all-carbocyclic Zr-MOF counterparts, Zr-TSS-1 shows a substantial improvement in visible-light harvesting and free-carrier generation, enabling it to be a promising candidate for photocatalytic antibacterial applications. In order to validate the advantages of this framework as an antibacterial protective material, a composite was fabricated by incorporating robust Zr-TSS-1 onto sustainably accessible bacterial cellulose (BC) using an in situ growth method. This composite exhibits near-complete lethality toward typical Gram-negative *Escherichia coli* and Gram-positive *Staphylococcus aureus* within 1 h under mild irradiation and preserves outstanding antibacterial capability after five cycles of reutilization. In addition, the high biocompatibility is confirmed by the low cytotoxicity toward human skin fibroblast, suggesting its potential for biomedical and healthcare applications. This research demonstrates the efficacious integration of a purposely designed photosensitive porous framework onto a sustainable substrate for synergistic functionality, paving a practical way for the development of the next-generation high-efficiency antimicrobial technology.

metal-organic frameworks | reticular chemistry | photocatalytic antibacterial method

Infectious pathogens like bacteria and viruses have posed a huge risk to the health of humankind for a long time. The latest case—the sudden outbreak of COVID-19—caught people off guard and posed a serious threat to public security and economic progress (1, 2). Moreover, it has been reported that many patients, infected clinically with COVID-19, suffered from secondary bacterial infections and attack from drug-resistant bacteria (3). As a result, efficient inactivation of infectious pathogens and inhibition of their secondary or even multiple transmissions are in high demand (4). The photocatalytic antimicrobial method is considered an attractive solution to lessen the menace of high-risk pathogens (1, 5). The efficient inactivation of microbes is achieved by photoinduced reactive oxygen species (ROS) with good oxidative capacity and little side effects. Also, the photocatalysts play a pivotal role in the generation of ROS, which determines the antibacterial efficiency during photocatalysis (1, 5). Therefore, it is of importance to design high-performance and biologically compatible materials for photocatalytic sterilization.

Metal-organic frameworks (MOFs), composed of organic and inorganic building blocks, have recently attracted much attention in various applications owing to their controllable structures and adjustable functionalities, including gas storage and separation, sensing and catalysis, as well as biomedical applications (6–11). Zirconium-based MOFs (Zr-MOFs) are one of the most explored MOFs owing to their high thermal, chemical, and mechanical stabilities (12). Recently, Zr-MOFs have been applied extensively in the photocatalysis field thanks to their tunable structures (13–16). Organic molecules containing multiple thiophene units are employed commonly in the design of efficient perovskite solar cells and fluorescent sensors (17–19). It is worth noting that photosensitive Zr-MOFs, constructed with ligands containing functional tetrathienylethene units, have yet to be explored (20, 21). In addition, the realization of functional composites for practical antibacterial applications requires the successful integration of photosensitive materials onto suitable substrates (22–24). In some previous studies, light-driven protective composites have been prepared by incorporating typical ZIF-8 and CAU-1 onto fabrics (25, 26). Another photocatalytic antibacterial composite has been prepared by embedding microcrystalline NU-1012 onto cotton cloths (27). It remains a challenge, however, to fabricate desirable MOF-based composites based on

Significance

Infectious pathogens, such as viruses and bacteria, pose a huge threat to human daily life, photocatalytic antibacterial method has been considered as an effective solution. Metal-organic frameworks (MOFs), known as attractive photocatalysts, are desirable candidates for photocatalytic antibacterial applications. Herein, we have designed and prepared a photoactive and stable MOF-based composite by introducing photosensitive ligand with tetrathienylethene unit. Compared with all-carbocyclic MOF counterparts, the tetrathienylethene-based MOF exhibits stronger visible-light harvesting and quicker production of abundant free carriers. Additionally, the biosafe composite shows near-complete bacterial-killing activity against *Staphylococcus aureus* and *Escherichia coli* within 1 h. This investigation provides a good proof-of-principle for constructing a biocompatible antibacterial composite and offers a direction to shape the next era of antibacterial arsenals.

The authors declare no competing interest.

This article is a PNAS Direct Submission.

[1]S.M. and Y.L. contributed equally to this work.

[2]To whom correspondence may be addressed. Email: kan.chi.wai@polyu.edu.hk, kaikai.ma@polyu.edu.hk, or zhijiechen@zju.edu.cn.

This article contains supporting information online at https://www.pnas.org/lookup/suppl/doi:10.1073/pnas.2423052122/-/DCSupplemental.

Published April 7, 2025.

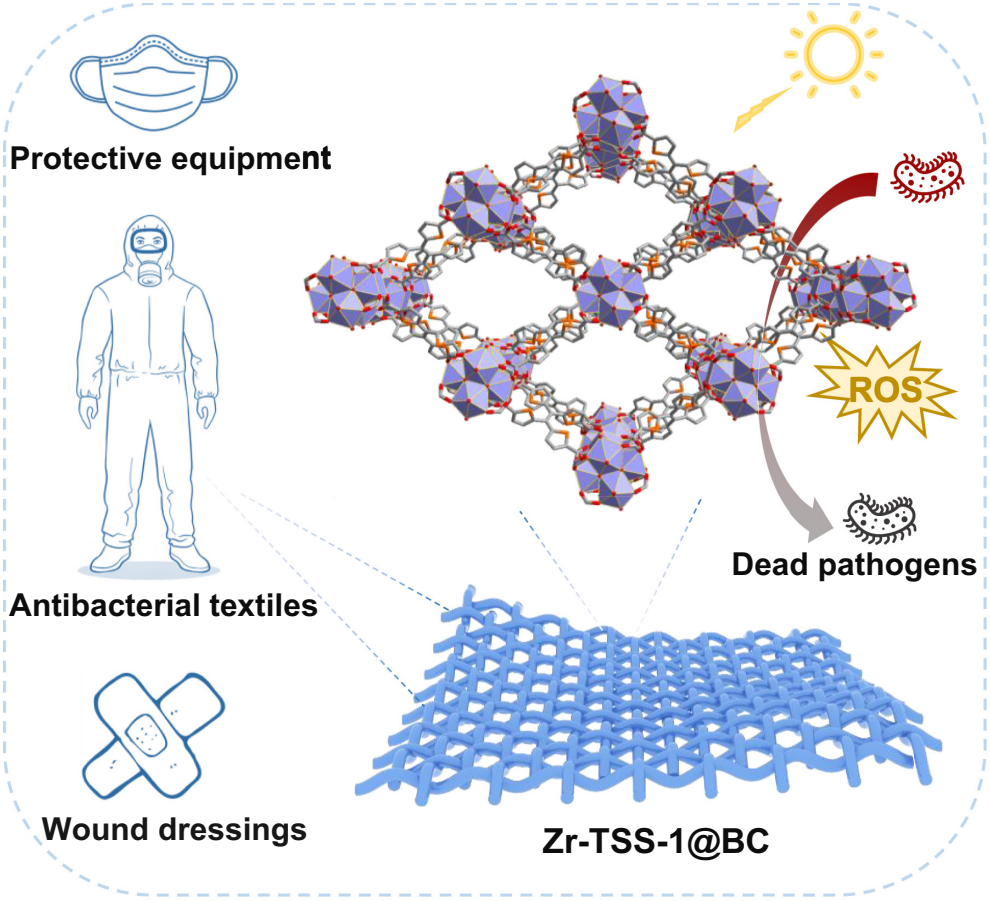

Scheme 1. The schematic diagram of antibacterial fibers containing Zr-TSS-1 with promising practical applications.

molecular-level design (1, 28, 29). Moreover, the bioavailability of MOF-based composites, which has been less explored, is significant when it comes to their practical adoption in healthcare-related applications (1, 29).

In this context, we have designed and constructed a stable and photoactive Zr-MOF—Zr-TSS-1—by introducing a photoresponsive tetrathienylethene-based linker [TSS-1 = 5,5′,5″,5‴-(ethene-1,1,2,2-tetrayl)tetrakis(thiophene-2-carboxylic acid)]. In comparison to the representative all-carbocyclic MOFs with analogous topological networks, like Zr-TCPE and NU-903 [TCPE = 1,1,2,2-tetra(4-carboxyl-phenyl)ethylene, NU = Northwestern University], the as-prepared Zr-TSS-1 with multiple functional thiophene units exhibits stronger visible-light capture and quicker carrier separation and transport, implying excellent photocatalytic applicability. In order to solve the inconvenience of employing powdery MOFs in practical applications, we embedded microcrystalline Zr-TSS-1 onto porous bacterial cellulose (BC) in order to fabricate (Scheme 1) a photoactive composite—Zr-TSS-1@BC. In line with our expectations, the Zr-TSS-1@BC displays outstanding inactivation to *Escherichia coli* and *Staphylococcus aureus*. In addition, insignificant changes in antibacterial activity of the composite were found after consecutive reuse. More importantly, this composite causes negligible damage to living mammalian cells in cytotoxicity assays, confirming its suitability for the manufacture of protective equipment, antibacterial textiles, and wound dressings.

Results and Discussion

Synthesis and Structural Analysis. In contrast to a plethora of TPE-based MOFs (TPE = tetraphenylethene) (30), tetrathienylethene (TTE) with a similar structure to classic TPE (31) has yet to be introduced into MOF-based materials, potentially because of the challenging synthetic procedure. In addition, TTE with its four photosensitive thiophene units is ideal for the use of visible light, making it a promising building block for the construction of porous MOF-based photocatalysts (32, 33). Herein, we have designed a carboxylate-based organic ligand (TSS-1) using TTE as the core unit. It was prepared by the reaction of CO_2 with lithiated TTE under anhydrous and anaerobic conditions. Next, we decided to construct a stable Zr-MOF according to the principles of reticular chemistry and the theory of Hard–Soft Acid–Base (6, 13) (HSAB). A solvothermal reaction of TSS-1 and $ZrCl_4$ in *N*,*N*-dimethylformamide with formic acid as a modulator affords (Fig. 1*A* and *SI Appendix*, Fig. S2) yellowish single crystals of Zr-TSS-1 under optimal conditions (*SI Appendix*, Table S1). Single-crystal X-ray diffraction analyses reveal that Zr-TSS-1 crystallizes in the orthorhombic space group *Ibam* with the lattice parameters a = 28.2838(6), b = 18.9646(4), c = 19.9599(4) Å (*SI Appendix*, Table S2) at 193 K. Each TSS-1 is connected to four Zr_6 clusters, while each cluster is coordinated with eight carboxylates from eight different linkers. Adjacent Zr_6 clusters are reinforced by two in situ inserted formates (FAs), forming a robust network (Fig. 1*A* and *SI Appendix*, Fig. S3–S5) similar to that in the reported (34–36) NU-901-NDC, PCN-224-BPDC, and MTV-MOFs, synthesized by postmodification. The unsaturated sites in the Zr_6 clusters are occupied by four FA molecules. We identified the formula of Zr-TSS-1 to be $[Zr_6O_8(FA)_6(TSS\text{-}1)_2]$, which is also supported by ^{1}H NMR spectroscopy (*SI Appendix*, Fig. S6) carried on digested Zr-TSS-1. In addition, the structure contains (Fig. 1*B*) two pockets, one of which is a vacant diamond-shaped channel viewed along the *c*-axis, while the other is segmented by FAs viewed in the direction of the *b*-axis.

Topologically, if the FAs bridging adjacent Zr_6 clusters are omitted, the TSS-1 linkers can be simplified as square blocks which link

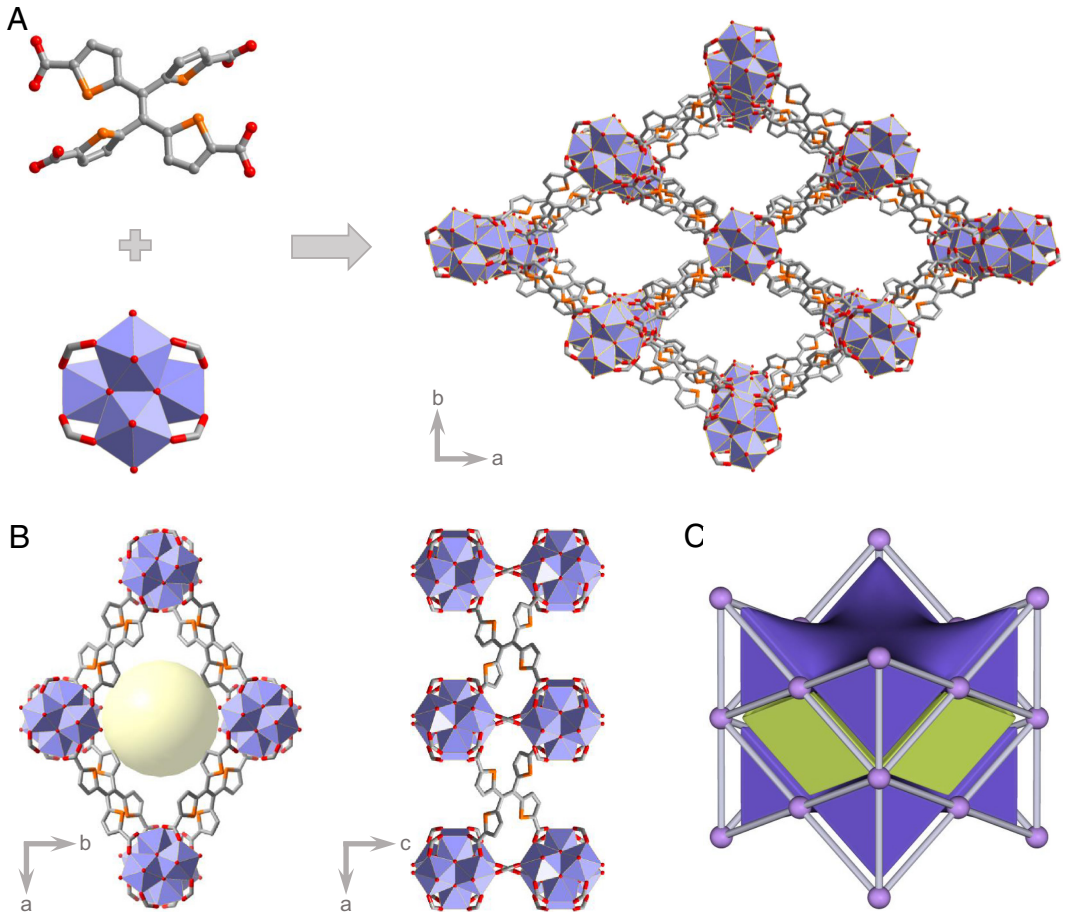

Fig. 1. Structural illustration of Zr-TSS-1. (*A*) The construction of Zr-TSS-1 from Zr_6 cluster and TSS-1 ligand. The single net of Zr-TSS-1 viewed along the *c*-axis. (*B*) The illustration of pockets in Zr-TSS-1 viewed along the *c*- and *b*-axis. (*C*) The natural tiling of 3D structure in Zr-TSS-1. Zr light purple, C gray, O red, and S orange. H atoms are omitted for the sake of clarity.

to the clusters to form a (4, 8)-connected **scu** net (37) (*SI Appendix*, Fig. S4). Alternatively, the underlying network of Zr-TSS-1 can be analyzed as a (4, 10)-connected **sqc246** net, if the Zr_6 clusters are simplified as 10-connected nodes while the FAs can be considered as linkers (38) (*SI Appendix*, Fig. S7). In addition, the three-dimensional (3D) structure of Zr-TSS-1, visualized intuitively by 3dt software (39), contains two types of tiles with a transitivity of [2332] in the **sqc246** net (Fig. 1*C*).

Characterization and Chemical Stability. The phase purity of bulk samples of Zr-TSS-1 was validated (Fig. 2*A* and *SI Appendix*, Fig. S8) by a high congruence of simulated and experimental powder X-ray diffraction (PXRD) patterns. Scanning electron microscope (SEM) images reveal the tablet-like morphology of the microcrystalline Zr-TSS-1 (*SI Appendix*, Figs. S9 and S10). SEM equipped with energy dispersive X-ray spectroscopy (EDX) system was used to determine the distribution of C, O, Zr, and S element in Zr-TSS-1 (*SI Appendix*, Fig. S11). Additionally, the X-ray photoelectron spectroscopy (XPS) illustrates the presence and chemical state of C, O, Zr, and S in Zr-TSS-1 (*SI Appendix*, Fig. S12). The high-resolution XPS of Zr 3d can be deconvoluted into two peaks for Zr $3d_{5/2}$ and Zr $3d_{3/2}$ at 182.6 and 184.9 eV, respectively (*SI Appendix*, Fig. S12*C*). The high-resolution XPS of C 1 s, S 2p, and O 1 s were identified to prove the structure of Zr-TSS-1 (*SI Appendix*, Fig. S12). Moreover, the permanent porosity is evaluated by N_2 adsorption–desorption isotherms at 77 K, confirming the microporous nature of Zr-TSS-1 (37) (Fig. 2*B*). The apparent Brunauer–Emmett–Teller surface area was calculated to be 950 $m^2\ g^{-1}$, and the experimental total pore volume was estimated to be 0.45 $cm^3\ g^{-1}$ at $P/P_0 = 0.95$, matching the theoretical pore volume of 0.46 $cm^3\ g^{-1}$. In addition, we have assessed the chemical stability and thermal resistance, as these properties are important for the photocatalytic applications of Zr-TSS-1. The PXRD patterns of Zr-TSS-1 are almost unchanged (Fig. 2*C*) after exposure to aqueous solutions with pH values ranging from 1 to 11. The framework, morphology, and particle size of Zr-TSS-1 after treatment were evaluated by N_2 sorption, PXRD, and SEM characterizations (*SI Appendix*, Figs. S13–S15). These results indicate that the crystalline framework and micromorphology of Zr-TSS-1 can generally be retained at different pH, implying that Zr-TSS-1 has good acid and base resistance (40). Furthermore, the crystalline structure and porous framework are retained after activation from water (*SI Appendix*, Figs. S16 and S17), suggesting its high hydrolytic stability (41). Additionally, the thermal stability of Zr-TSS-1 exceeds 200 °C according to N_2 adsorption isotherms activated at different temperatures (Fig. 2*D*). The thermogravimetric analysis of Zr-TSS-1 suggests that its decomposition temperature under air flow is about 300 °C (*SI Appendix*, Fig. S18). These results show that Zr-TSS-1 is a stable material for further manufacture and practical use.

Photoelectric Properties and Band Structures. We investigated the photoelectric properties of Zr-TSS-1, which are critical for the determination of photocatalytic capability (42, 43). For comparison, we also prepared (*SI Appendix*, Fig. S19) two typical all-carbocyclic Zr-MOFs (Zr-TCPE and NU-903) with

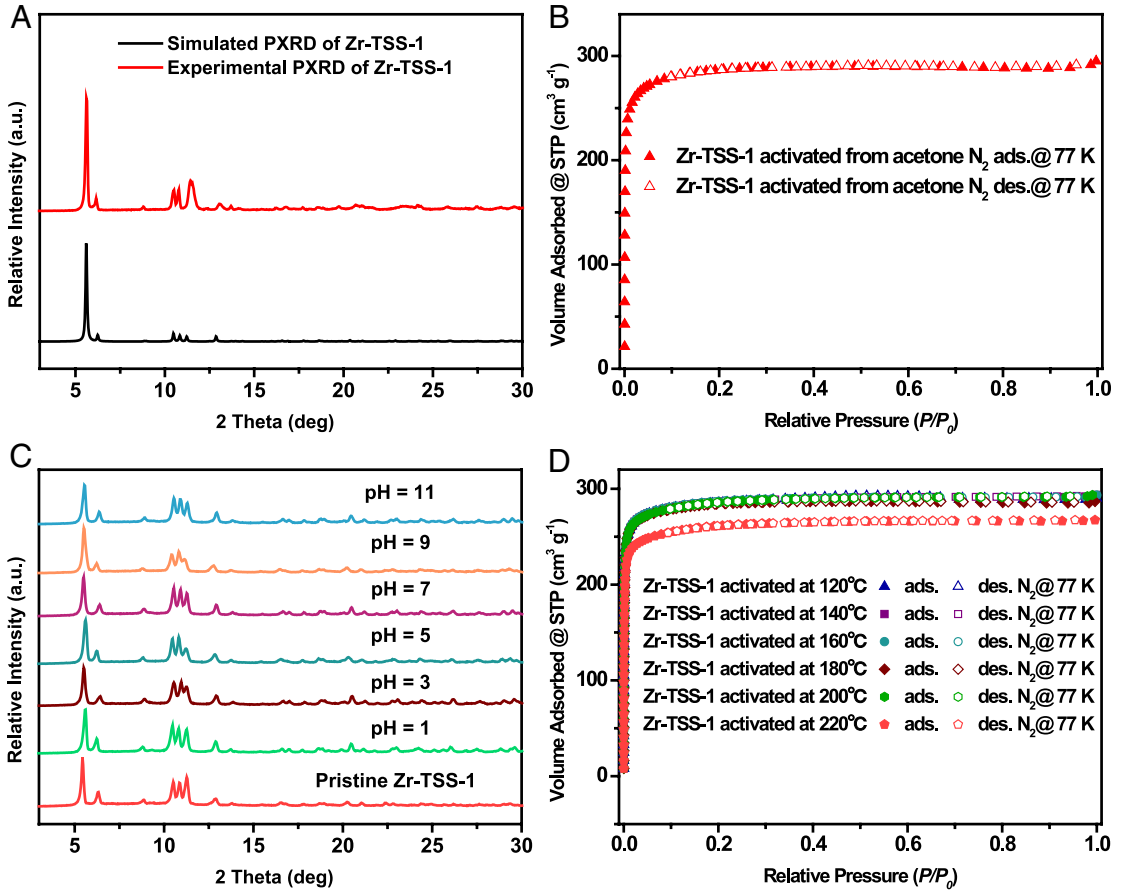

Fig. 2. (*A*) Experimental and simulated PXRD patterns of Zr-TSS-1. (*B*) Nitrogen sorption isotherm profile of Zr-TSS-1. (*C*) PXRD patterns of Zr-TSS-1 after exposure to aqueous solutions with pH values ranging from 1 to 11. (*D*) N_2 sorption isotherms of Zr-TSS-1 activated at different temperatures.

analogous topologies to Zr-TSS-1 according to the literature (44, 45). The PXRD patterns (*SI Appendix*, Fig. S20) of as-prepared microcrystalline powders are well matched with those of the simulated structures. UV/Vis diffuse reflectance spectroscopic measurements of the as-prepared samples indicate that Zr-TCPE and NU-903 exhibit (420 nm) mainly narrow optical absorbance within the blue edge of the visible light spectrum. In contrast, a broader absorbance extending to about 500 nm was acquired (Fig. 3*A*) by Zr-TSS-1 through the introduction of tetrathienylethene. This observation suggests that higher visible-light utilization and more photogenerated exciton formation can be achieved (46, 47). Besides, the photocurrent density of Zr-TSS-1 was measured to be about three- to four-fold higher than those of Zr-TCPE and NU-903 (Fig. 3*B*), implying more efficient photoinduced charge separation and transfer for photocatalysis (48, 49). Additionally, the photocurrent density of Zr-TSS-1 also surpassed that of its ligand—TSS-1 (*SI Appendix*, Fig. S21), suggesting the advantage of porous framework for high-efficiency charge transfer (50). To this end, the findings are aligned with our design concept, indicating that this Zr-TSS-1 with a strong visible-light response and good photoelectric properties is a promising photocatalyst.

Furthermore, the optical energy gap (E_g) of Zr-TSS-1 is determined to be 2.51 eV from a Tauc plot (*SI Appendix*, Fig. S22). To confirm the band energy structure, Mott–Schottky (M–S) plots were employed to estimate the energy level of the conduction band minimum (51) (E_{CB}). Based on the M-S plots (Fig. 3*C*), the E_{CB} of Zr-TSS-1 is about −0.83 V vs. Ag/AgCl, corresponding to −0.63 V vs. NHE (Normal Hydrogen Electrode). Thus, the energy level (E_{VB}) of the valence band maximum of Zr-TSS-1 is calculated (Fig. 3*D*) to be 1.88 V vs. NHE according to the equation (42) of $E_g = E_{VB} - E_{CB}$. With respect to the energy level necessary for generating common ROS-like $\bullet O_2^-$ and •OH, the conduction band (CB) of Zr-TSS-1 meets the required potential for producing $\bullet O_2^-$. The valence band (VB) of Zr-TSS-1, however, is unfavorable for the generation of •OH. The findings imply (Fig. 3*D*) that Zr-TSS-1 possesses sufficient driving force for some type of photoinduced ROS generation, suggesting its potential as a photocatalytic antimicrobial agent (1). For the purpose of comparing the ability of Zr-TSS-1 to produce ROS with those of two all-carbocyclic Zr-MOFs, nitro-blue tetrazolium (NBT) and furfuryl alcohol (FFA) were selected to indicate the $^1O_2$ and $\bullet O_2^-$ generation kinetics (*SI Appendix*, Fig. S23), respectively. The results suggest that Zr-TSS-1 has the highest $^1O_2$ and $\bullet O_2^-$ generation rate, implying its high antibacterial activity as we can predict (52, 53).

Preparation and Characterization of the Composite. We have fabricated protective materials by integrating photosensitive Zr-MOFs onto sustainable substrates, yielding excellent light-driven self-cleaning effects. Among various substrates, BC is well known as a porous, biocompatible, and biodegradable natural polymer (54). Its 3D network possesses acceptable surface areas with hydroxyl groups, which are beneficial for water retention and filler loading. Its hydrophilic characteristics contribute to its high wettability, and thus ensuring wear comfort (54).

BC, owing to its exceptional porousness, biodegradation, biocompatibility, flexibility, rigidity, and durability (55–57), is considered as a support for embedding microcrystals to produce functional materials. Next, we incorporated microcrystalline Zr-TSS-1 onto the porous BC (Zr-TSS-1@BC) by adopting an

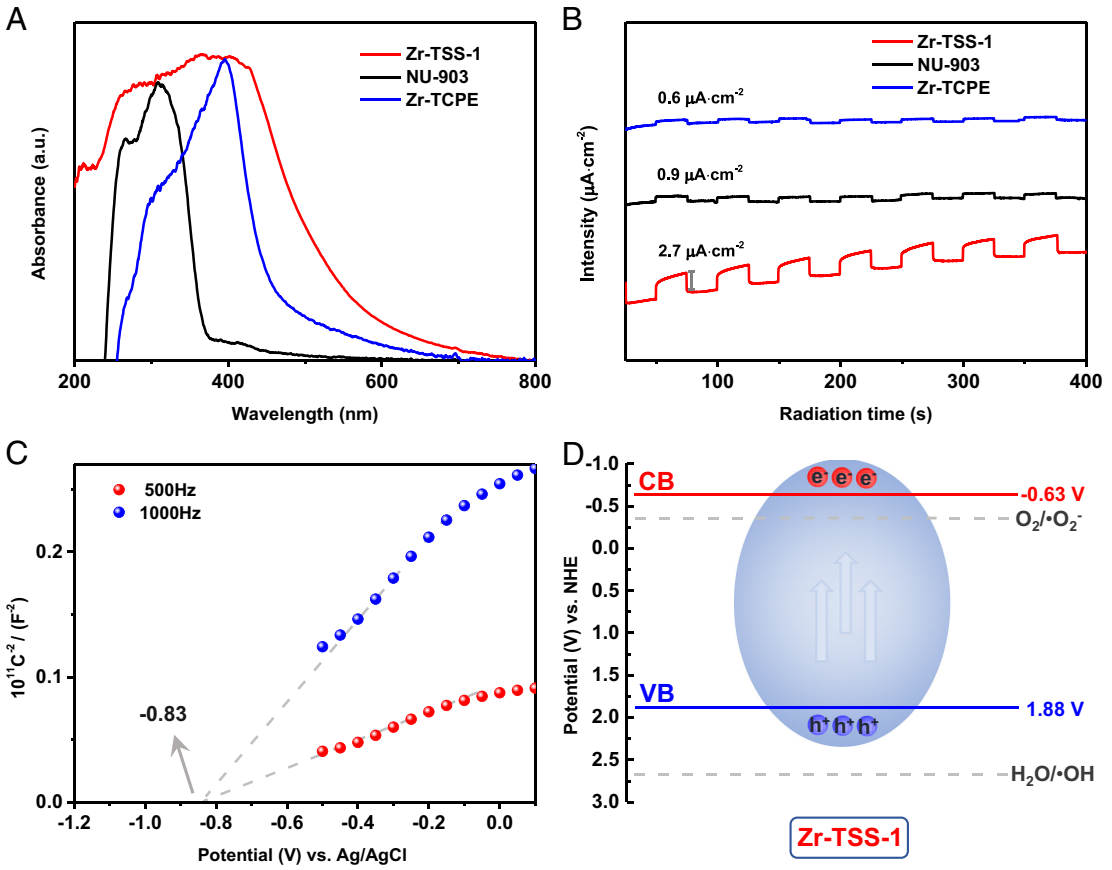

Fig. 3. (*A*) UV/Vis diffuse reflectance spectra of Zr-TSS-1, Zr-TCPE, and NU-903. (*B*) Photocurrent generated from Zr-TSS-1, Zr-TCPE, and NU-903 under intermittent irradiation. (*C*) Mott–Schottky plots for Zr-TSS-1. (*D*) The band structure of Zr-TSS-1 with respect to the driving force of ROS.

in situ growth method (27), suggested by the well-matched PXRD pattern (Fig. 4*A*) to that of Zr-TSS-1 microcrystals. SEM images taken from the surface and cross-section of Zr-TSS-1@BC show (Fig. 4 *B* and *C* and *SI Appendix*, Fig. S24) that the microcrystals are distributed regularly in the 3D microstructure, which is distinct from that of pristine BC (*SI Appendix*, Fig. S25). Elemental mappings using SEM-EDX reveal the uniform distribution of Zr-TSS-1 on the BC substrate (*SI Appendix*, Fig. S26). Overall, the microfibrils and porous network of BC can lessen the agglomeration of microcrystals.

Additionally, the mechanical properties of BC and Zr-TSS-1@BC were assessed at nanoscale by atomic force microscope (*SI Appendix*, Fig. S27). The findings demonstrate that the Young's modulus of the composite is ~13.5 GPa while that of pure BC is about 9.5 GPa, suggesting the brittleness slightly increases after loading of Zr-TSS-1 onto BC (58, 59).The composite shows good mechanical strength (Fig. 4*B*, *Inset*) potentially on account of the supramolecular and interfacial interactions (4, 22) between Zr-TSS-1 and BC. Concomitantly, the color change from white to yellow was observed visually (*SI Appendix*, Fig. S28). The water contact angle of BC materials was measured at the moment of applying a water droplet onto the surfaces of specimens (*SI Appendix*, Fig. S29). BC retains good surface wettability after incorporating Zr-TSS-1, ensuring wear comfort (54). The smaller contact angle also implies better contact between bacterial suspensions and composites (60). The N_2 sorption isotherms of Zr-TSS-1@BC suggest that Zr-TSS-1@BC has a similar microporosity as powdery Zr-TSS-1 (*SI Appendix*, Fig. S30). The adsorbed volume closely relates to the loading of Zr-TSS-1 on the composites, and Zr-TSS-1@BC has a mass loading of about 57.3 wt% deduced from the results measured by inductively coupled plasma-optical emission spectroscopy (27). These results suggest that the porous BC structure allows good distribution of powdery Zr-TSS-1, and it also has no obvious negative impact on the microcrystals.

Antibacterial Activity and Biosafety Assessment. We have evaluated the antibacterial performance of the as-prepared composites against representative Gram-negative *E. coli* and Gram-positive *S. aureus* in the light of the modified version of AATCC 100:2019–Test Method for Antibacterial Finishes on Textile Materials (29, 61). In detail, 10 μL of activated bacterial strains were incubated separately on pure BC and Zr-TSS-1@BC under visible-light irradiation with a light intensity of ~4.71 W/m^2 for 1 h. This MOF-based composite exhibits (Fig. 4*D*) nearly 100 % inactivation of *E. coli* and *S. aureus* while pure BC poses few threats to both microbes. Its antibacterial efficiency under mild irradiation is comparable to those of MOF-related materials under harsher conditions reported previously (25, 27, 62–65) (*SI Appendix*, Table S3). Moreover, the crystallinity of the composite remains unchanged after consecutive photocatalytic cycles as proved by the unchanged PXRD patterns (*SI Appendix*, Fig. S31). Encouraged by the good stability of Zr-TSS-1, five cycles of antibacterial experiments were conducted. The results show that Zr-TSS-1@BC demonstrates enduringly high antibacterial efficiency against *E. coli* for over five consecutive cycles (Fig. 4*E* and *SI Appendix*, Fig. S32), suggesting Zr-TSS-1 microcrystals are firmly anchored onto the porous BC. The photocatalytic efficiency of three different batches of composites to *E. coli* was evaluated. The findings show that different batches of composites have similar antibacterial activity, indicating good batch-to-batch reproducibility (*SI Appendix*, Figs. S33 and S34). Additionally, control experiments imply that Zr-TSS-1@BC induce limited damage to *E. coli* in the absence of light (*SI Appendix*, Fig. S35). In order to understand the

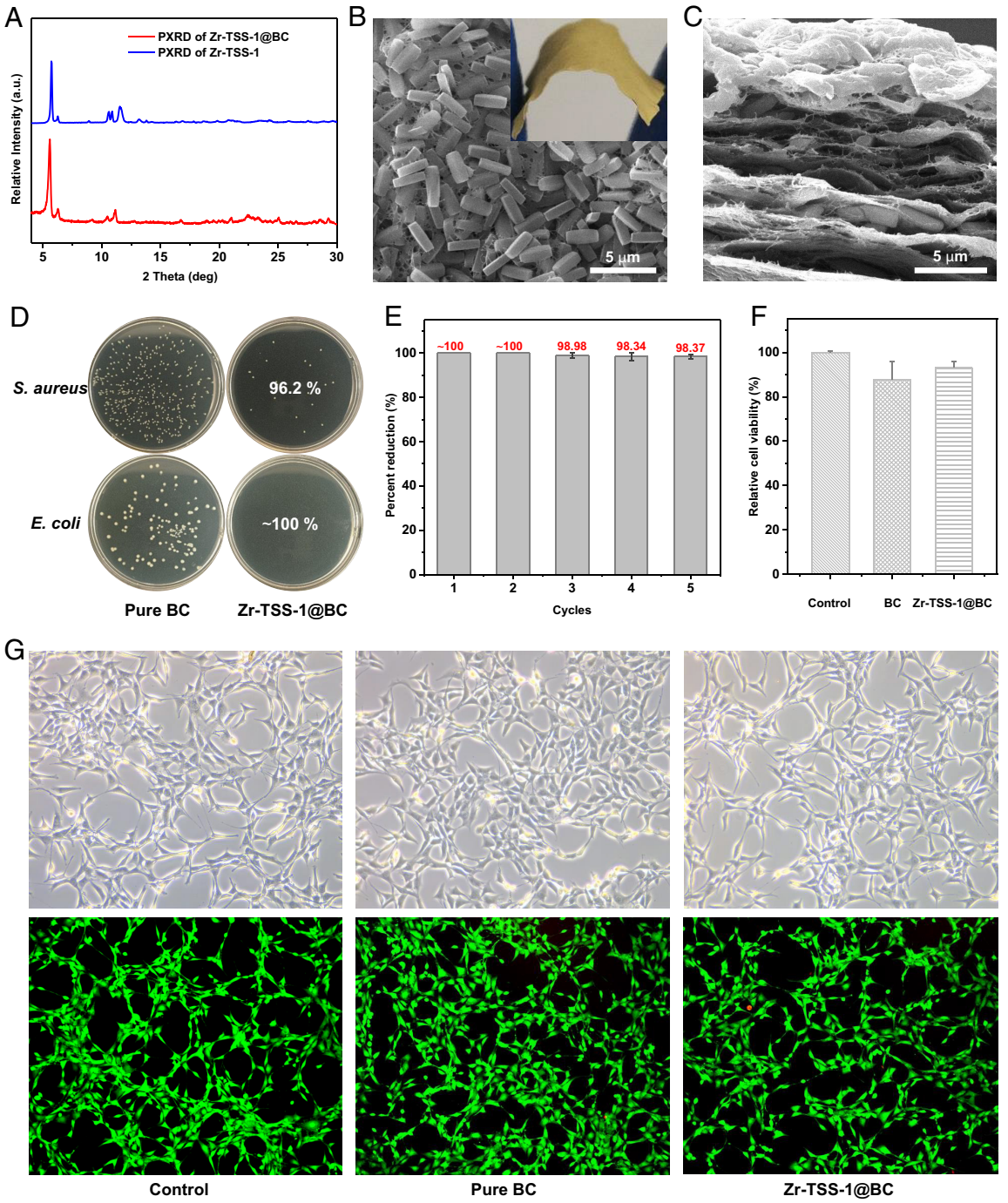

Fig. 4. (*A*) Comparison of experimental PXRD of Zr-TSS-1 and Zr-TSS-1@BC. (*B*) SEM images of Zr-TSS-1@BC from surface section, *Inset*: photograph of flexible composite with good mechanical strength. (*C*) SEM images of Zr-TSS-1@BC from cross-section. (*D*) Photographs of *Staphylococcus aureus* and *Escherichia coli* incubated with Zr-TSS-1@BC and pure BC under visible-light irradiation for 1 h (1:10000 dilution). (*E*) Antibacterial efficiency against *E. coli* for five consecutive cycles. (*F*) The relative cell viability of human skin fibroblasts after 24 h incubation. (*G*) Confocal micrographs: bright-field and merged fluorescent images of Calcein AM/PI-stained NIH-3T3 fibroblasts after 24 h incubation with blank, pure BC, and Zr-TSS-1@BC. (Scale bar, 100 mm.)

photocatalytic mechanism, electron paramagnetic resonance (EPR) measurements were performed on Zr-TSS-1. The characteristic peaks of DMPO-•O_2^- and TEMP-$^1O_2$ were acquired under irradiation while no signals were observed under dark conditions (*SI Appendix*, Fig. S36). This finding suggests that •O_2^- and $^1O_2$ play a critical role in the light-driven antibacterial activity. We assume that •O_2^- and $^1O_2$ could stem mainly from the metal-to-ligand charge transfer (MLCT) process in Zr-TSS-1 according to the combined experimental and calculation results (*SI Appendix*, Fig. S37 and S38) (66, 67). The ROS most likely oxidizes the biomolecules of bacterial cell walls and cell membranes, inducing the death of the bacteria (28). Besides, the porous framework of BC enables the Zr-TSS-1 to disperse on the substrate uniformly, exposing more surfaces for light- harvesting and bacterial contact. Thus, the excellent antibacterial efficiency of the composite is realized by the synergy of visible-light responsive Zr-TSS-1 and porous BC.

The biosafety of MOFs should be given careful consideration when it comes to biomedical applications in healthcare-related fields (1). Hence, we have evaluated the bioavailability of Zr-TSS-1@BC via 3-(4,5-dimethylthiazol-2-yl)-2,5-diphenyltetrazolium bromide (MTT) assay, an extensively adopted method for sensitive detection of cell growth and survival (68). The relative cell viability of human

skin and NIH 3T3 fibroblasts after 24 h incubation with the composite reveals that Zr-TSS-1 has weak cytotoxic activity toward living mammalian cells (69) (Fig. 4*F* and *SI Appendix*, Fig. S39 and S40). The bright-field confocal microscopic images of human skin and NIH 3T3 fibroblasts also confirm visually that the cell morphologies have suffered no obvious damage after exposure to the composite (Fig. 4*G* and *SI Appendix*, Fig. S41). Moreover, the merged fluorescent images of Calcein AM/PI-stained human skin and NIH 3T3 fibroblasts among experimental and control groups suggest that little harm is inflicted by the composites on living cells owing to its low cytotoxicity (70, 71) (Fig. 4*G* and *SI Appendix*, Fig. S42). Overall, the Zr-TSS-1@BC displays good biocompatibility and is a desirable photocatalytic antibacterial platform.

Conclusions

An advanced photosensitive composite—Zr-TSS-1@BC—has been designed and prepared by incorporating a stable Zr-MOF to sustainable and highly durable BC as a result of in situ growth. The as-prepared composite achieves an exceptional antibacterial efficiency against *E. coli* and *S. aureus* on account of photogenerated $\bullet O_2^-$ and $^1O_2$, which can be attributed to the strong visible-light response and excellent photoelectric properties of Zr-TSS-1 as well as to its regular distribution on porous BC. Thanks to the good chemical stability and high thermal tolerance of Zr-TSS-1, this composite displays a long-lasting and effective bacterial killing serviceability in multiple reuse scenario. Despite this remarkable efficiency, cytotoxicity assessment reveals that the composite demonstrates hypotoxicity with acceptable biocompatibility. These findings prove that Zr-TSS-1@BC has a bright future for practical applications including protective equipment, antibacterial textiles, and wound dressings. Our investigation provides an example of designing a bioavailable composite at the molecular level, and offers a viewpoint to shape the next era of antibacterial arsenals.

Materials and Methods

Chemicals and Materials. All reagents were obtained from commercial sources and used without further purification or treatment, unless otherwise noted. BC hydrogel was prepared from commercially available Nata de Coco (Kara Santan Pertama, Bogor 16964, Indonesia). 1,1,2,2-tetra(4-carboxylphenyl) ethylene (TCPE) and 1,2,4,5-tetrakis(4-carboxyphenyl)benzene were obtained from Shanghai Bide Pharmaceutical Technology Co., Ltd. Mouse fibroblasts (iCell-m041) were derived from mouse embryos and human fibroblasts (iCell-0051a) were derived from human dermal tissue, both of which were purchased from iCell Bioscience Inc, Shanghai.

Characterization. General characterization procedures are provided in *SI Appendix*.

The Synthesis of Single Crystals of Zr-TSS-1. TSS-1 (2 mg) and $ZrCl_4$ (4 mg) were added into a 15 mL vial, followed with 2 mL *N*,*N*-dimethylformamide (DMF) and formic acid (0.6 mL). Then, the mixture was sonicated for 2 mins, heated up to 130 °C, and maintained for 20 h. After returning to room temperature, yellow single crystals were washed with fresh DMF twice for single crystal X-ray diffraction measurements.

The Synthesis of Microcrystalline Zr-TSS-1. TSS-1 (30 mg), $ZrOCl_2{\cdot}8H_2O$ (60 mg), 2 mL DMF, and formic acid (0.6 mL) were added sequentially into 15 mL vial. Then, the mixture was sonicated for 2 mins, heated up to 130 °C, and maintained for 20 h. After returning to room temperature, the polycrystalline powders were collected by centrifugation and washed with fresh DMF twice. Then, the obtained samples were soaked in DMF and replaced with fresh DMF every 12 h in 2 d, further soaked in acetone and replaced with fresh acetone every 12 h in 2 d. Ultimately, the target powders were dried in a vacuum oven at 60 °C overnight and ready for subsequent characterization or performance tests.

Synthesis of Zr-TSS-1/Bacterial Cellulose Composite (Zr-TSS-1@BC). Under optimal conditions, BC (4 g), $ZrOCl_2$ (60 mg, 186.19 μmol), and TSS-1 (30 mg, 56.33 μmol) were added to DMF (1 mL) in glass vial. To ensure uniform distribution of metal clusters and linkers within the BC, the mixture was first subjected to ultrasonic treatment for homogenization. Formic acid (3 mL, 65.17 mmol) was added to the mixture in a ratio of 1:0.6 (DMF: formic acid) to modulate the growth of MOF crystals. BC with precursors then reacted at 130 °C for 15 h. The product was then collected and washed with DMF and acetone several times.

Antibacterial Efficiency Tests. With the presence of Zr-TSS-1-loaded on BCs, we then evaluated their antibacterial performance against Gram-negative bacteria *S. aureus* (ATCC 6538) and Gram-negative *E. coli* (CMCC 44102) according to the modified version of AATCC 100:2019 – Test Method for Antibacterial Finishes on Textile Materials. The antibacterial efficiency test is conducted with three parallel groups. The activated test bacterial strains were diluted to ~1.2 to 4.1 × 10^7 colony-forming units (CFU)/mL. 10 μL of each inoculum bacteria were added onto individual pristine BC and Zr-TSS-1@BC (1 piece, 1 cm × 1 cm), respectively. They were then irradiated under fluorescent lamp (PHILIPS TLD 18 W/865 YZ18RR25 COOLDAYLIGHT 6500 K) with a light intensity of ~4.71 W/m^2 for 1 h. Immediately after light irradiation, 990 μL of phosphate-buffered saline (PBS) was added to each specimen, and the solution was shaken vigorously for 1 min to rinse off the adhered bacteria. The solution with recovered bacteria was then serially diluted with PBS for agar plating, and the agar plates were then cultured at 37 °C for 18 h. The bacterial counts of specimens were then obtained, and the percent reduction was calculated according to the equation: R = 100 (B − A)/B, where R represents the percent reduction, A is the number of viable bacteria recovered from the treated specimen over the contact period, and B is the number of viable bacteria recovered from the untreated specimen over the contact period.

Data, Materials, and Software Availability. X-ray crystallographic coordinates for structures reported in this study data have been deposited in Cambridge Crystallographic Data Centre (CCDC) [2328617 (Zr-TSS-1), http://www.ccdc.cam.ac.uk/data_request/cif] (72). All study data are included in the article and/or *SI Appendix*.

ACKNOWLEDGMENTS. Z.C. gratefully acknowledges support from the National Natural Science Foundation of China (Grant no. 22201247 and 22471237), the Zhejiang Provincial Natural Science Foundation of China (No. LR25B010001), and startup funding from Zhejiang University. We thank the staff at BL17B1 beamline of the National Facility for Protein Science in Shanghai (NFPS), Shanghai Advanced Research Institute, CAS, for providing technical support in X-ray diffraction data collection and analysis. We thank Jiyong Liu from Chemistry Instrumentation Center Zhejiang University for the technical support. K.M. acknowledges the support from the start-up fund of the Hong Kong Polytechnic University (1-BDD2) and B.F. acknowledges the support from the Hong Kong Polytechnic University ESG Hub (1-WZ2H). C.K. acknowledges the grant funding provided by the Hong Kong Polytechnic University (R-ZDCC). J.H.X. acknowledges the support from General Research Fund of the Research Grants Council of the Hong Kong SAR Government (GRF 15208420). This work was supported by the Leading Innovative and Entrepreneur Team Introduction Program of Zhejiang (No. 2023R01007). This work was partially supported by the Key Research and Development Program of Zhejiang Province (No. 2025C02214). We thank Shiyanjia Lab (www.shiyanjia.com) for the support of AFM measurements. We thank Zuping Xiong for assisting in theoretical calculation.

Author affiliations: [a]Stoddart Institute of Molecular Science, Department of Chemistry, Zhejiang Key Laboratory of Excited-State Energy Conversion and Energy Storage, State Key Laboratory of Silicon and Advanced Semiconductor Materials, Zhejiang University, Hangzhou 310058, P. R. China; [b]Zhejiang-Israel Joint Laboratory of Self-Assembling Functional Materials, ZJU-Hangzhou Global Scientific and Technological Innovation Center, Zhejiang University, Hangzhou 311215, P. R. China; [c]Research Institute for Intelligent Wearable Systems, School of Fashion and Textiles, The Hong Kong Polytechnic University, Hung Hom, Hong Kong, Special Administrative Region of China; [d]Department of Chemistry, The University of Hong Kong, Hong Kong Island, Hong Kong, Special Administrative Region, P. R. China; [e]Weinberg College of Arts and Sciences, Northwestern University, Evanston, IL 60208; [f]Center for Regenerative Nanomedicine, Northwestern University, Chicago, IL 60611; and [g]School of Chemistry, University of New South Wales, Sydney, NSW 2052, Australia

Author contributions: K.M., J.F.S., and Z.C. designed research; S.M. and Y.L. performed research; L.S., C.K., B.F., and J.H.X. contributed new reagents/analytic tools; J.Y., K.W., B.Y., C.K., B.F., and J.H.X. analyzed data; and S.M., Y.L., C.K., K.M., J.F.S., and Z.C. wrote the paper.

1. B. Ran *et al.*, Photocatalytic antimicrobials: Principles, design strategies, and applications. *Chem. Rev.* **123**, 12371–12430 (2023).
2. B. Li *et al.*, Two-dimensional antibacterial materials. *Prog. Mater. Sci.* **130**, 100976–101028 (2022).
3. J. M. Farrell, C. Y. Zhao, K. M. Tarquinio, S. P. Brown, Causes and consequences of COVID-19-associated bacterial infections. *Front. Microbiol.* **12**, 682571 (2021).
4. K. Ma *et al.*, Protection against chemical warfare agents and biological threats using metal-organic frameworks as active layers. *Acc. Mater. Res.* **4**, 168–179 (2023).
5. J. Zeng, Z. Li, H. Jiang, X. Wang, Progress on photocatalytic semiconductor hybrids for bacterial inactivation. *Mater. Horiz.* **8**, 2964–3008 (2021).
6. Z. Chen, K. O. Kirlikovali, L. Shi, O. K. Farha, Rational design of stable functional metal–organic frameworks. *Mater. Horiz.* **10**, 3257–3268 (2023).
7. H. Y. Li *et al.*, Metalation of metal–organic frameworks: Fundamentals and applications. *Chem. Soc. Rev.* **53**, 5626–5676 (2024).
8. W. Gong, Z. Chen, J. Dong, Y. Liu, Y. Cui, Chiral metal-organic frameworks. *Chem. Rev.* **122**, 9078–9144 (2022).
9. L. Shi, Z. Xiong, H. Wang, H. Cao, Z. Chen, Quasicrystal approximants in isoreticular metal-organic frameworks via cairo pentagonal tiling. *Chem* **10**, 1–9 (2024).
10. R. B. Lin, Z. Zhang, B. Chen, Achieving high performance metal-organic framework materials through pore engineering. *Acc. Chem. Res.* **54**, 3362–3376 (2021).
11. Y. Qian, B. Li, M. Irfan, D. Li, H.-L. Jiang, Reactive oxygen species generation for catalysis and biotherapeutic applications based on crystalline porous materials. *Coord. Chem. Rev.* **518**, 216068–216107 (2024).
12. Y. Bai *et al.*, Zr-based metal-organic frameworks: Design, synthesis, structure, and applications. *Chem. Soc. Rev.* **45**, 2327–2367 (2016).
13. L. Shi, Z. Yang, F. Sha, Z. Chen, Design, synthesis and applications of functional zirconium-based metal-organic frameworks. *Sci. China Chem.* **66**, 3383–3397 (2023).
14. L. Feng, G. S. Day, K.-Y. Wang, S. Yuan, H.-C. Zhou, Strategies for pore engineering in zirconium metal-organic frameworks. *Chem* **6**, 2902–2923 (2020).
15. Z. Chen *et al.*, Reticular chemistry in the rational synthesis of functional zirconium cluster-based MOFs. *Coord. Chem. Rev.* **386**, 32–49 (2019).
16. J.-D. Xiao, H.-L. Jiang, Metal-organic frameworks for photocatalysis and photothermal catalysis. *Acc. Chem. Res.* **52**, 356–366 (2018).
17. H. Zhang *et al.*, Benzothieno[3,2-b]thiophene-based noncovalent conformational lock achieves perovskite solar cells with efficiency over 24. *Angew. Chem. Int. Ed.* **62**, e202314270 (2023).
18. H. Chen *et al.*, Terminally chlorinated and thiophene-linked acceptor-donor–acceptor structured 3D acceptors with versatile processability for high-efficiency organic solar cells. *Angew. Chem. Int. Ed.* **62**, e202307962 (2023).
19. J.-J. Liu *et al.*, Tetrathienylethene based red aggregation-enhanced emission probes: Super red-shifted mechanochromic behavior and highly photostable cell membrane imaging. *Mater. Chem. Front.* **2**, 1126–1136 (2018).
20. V. Bon, I. Senkovska, I. A. Baburin, S. Kaskel, Zr- and Hf-based metal–organic frameworks: Tracking down the polymorphism. *Cry. Growth Des.* **13**, 1231–1237 (2013).
21. N. Liu *et al.*, Two thiophene-functionalized Co-MOFs as green heterogeneous catalysts for the biginelli reaction. *Inorg. Chem.* **63**, 19117–19129 (2024).
22. K. Ma *et al.*, Fiber composites of metal-organic frameworks. *Chem. Mater.* **32**, 7120–7140 (2020).
23. A. M. Eagleton, E. K. Ambrogi, S. A. Miller, N. Vereshchuk, K. A. Mirica, Fiber integrated metal-organic frameworks as functional components in smart textiles. *Angew. Chem. Int. Ed.* **62**, e202309078 (2023).
24. G. W. Peterson, D. T. Lee, H. F. Barton, T. H. Epps, G. N. Parsons, Fibre-based composites from the integration of metal–organic frameworks and polymers. *Nat. Rev. Mater.* **6**, 605–621 (2021).
25. P. Li *et al.*, Metal-organic frameworks with photocatalytic bactericidal activity for integrated air cleaning. *Nat. Commun.* **10**, 2177 (2019).
26. J. Zhang, P. Li, X. Zhang, X. Ma, B. Wang, Aluminum metal–organic frameworks with photocatalytic antibacterial activity for autonomous indoor humidity control. *ACS Appl. Mater. Interfaces* **12**, 46057–46064 (2020).
27. X. Wang *et al.*, Photocatalytic biocidal coatings featuring Zr_6Ti_4-based metal-organic frameworks. *J. Am. Chem. Soc.* **144**, 12192–12201 (2022).
28. D. Han, X. Liu, S. Wu, Metal organic framework-based antibacterial agents and their underlying mechanisms. *Chem. Soc. Rev.* **51**, 7138–7169 (2022).
29. R. Li, T. Chen, X. Pan, Metal-organic-framework-based materials for antimicrobial applications. *ACS Nano* **15**, 3808–3848 (2021).
30. Y. Liu, X. Guan, Q. Fang, Recent advances in AIEgen-based crystalline porous materials for chemical sensing. *Aggregate* **2**, e34 (2021).
31. L. Viglianti *et al.*, Aggregation-induced emission: Mechanistic study of the clusteroluminescence of tetrathienylethene. *Chem. Sci.* **8**, 2629–2639 (2017).
32. V. Guillerm, D. Maspoch, Geometry mismatch and reticular chemistry: Strategies to assemble metal-organic frameworks with non-default topologies. *J. Am. Chem. Soc.* **141**, 16517–16538 (2019).
33. Y. Fang *et al.*, Design and synthesis of broadband absorption covalent organic framework for efficient artificial photocatalytic amine coupling. *Nat. Commun.* **15**, 4856–4864 (2024).
34. L. Robison *et al.*, Designing porous materials to resist compression: Mechanical reinforcement of a Zr–MOF with structural linkers. *Chem. Mater.* **32**, 3545–3552 (2020).
35. L. Zhang *et al.*, Cooperative sieving and functionalization of Zr metal–organic frameworks through insertion and post-modification of auxiliary linkers. *ACS Appl. Mater. Interfaces* **11**, 22390–22397 (2019).
36. X. Zhang, B. L. Frey, Y. S. Chen, J. Zhang, Topology-guided stepwise insertion of three secondary linkers in zirconium metal–organic frameworks. *J. Am. Chem. Soc.* **140**, 7710–7715 (2018).
37. R. R. Liang *et al.*, Exceptionally high perfluorooctanoic acid uptake in water by a zirconium-based metal–organic framework through synergistic chemical and physical adsorption. *J. Am. Chem. Soc.* **146**, 9811–9818 (2024).
38. M. J. Hurlock *et al.*, Evolution of 14-connected Zr_6 secondary building units through postsynthetic linker incorporation. *ACS Appl. Mater. Interfaces* **13**, 51945–51953 (2021).
39. O. Delgado-Friedrichs, M. O'Keeffe, Identification of and symmetry computation for crystal nets. *Acta Crystallogr., Sect. A: Found. Crystallogr.* **59**, 351–360 (2003).
40. R. R. Liang *et al.*, Zirconium-based metal–organic frameworks with free hydroxy groups for enhanced perfluorooctanoic acid uptake in water. *Adv. Mater.* **36**, e2407194 (2024).
41. B. Wang *et al.*, Highly stable Zr(IV)-based metal–organic frameworks for the detection and removal of antibiotics and organic explosives in water. *J. Am. Chem. Soc.* **138**, 6204–6216 (2016).
42. S. Ma *et al.*, Photocatalytic hydrogen production on a sp^2-carbon-linked covalent organic framework. *Angew. Chem. Int. Ed.* **61**, e202208919 (2022).
43. S. Ma, Y. Lam, L. Shi, K. Ma, Z. Chen, Stable MOFs and composites for photocatalytic antibacterial applications. *Trends Chem.* **6**, 712–725 (2024).
44. S. S. Meng *et al.*, Anisotropic flexibility and rigidification in a TPE-based Zr-MOFs with scu topology. *Nat. Commun.* **14**, 5347 (2023).
45. J. Lyu *et al.*, Topology and porosity control of metal-organic frameworks through linker functionalization. *Chem. Sci.* **10**, 1186–1192 (2019).
46. F. M. Zhang *et al.*, Rational design of MOF/COF hybrid materials for photocatalytic H_2 evolution in the presence of sacrificial electron donors. *Angew. Chem. Int. Ed.* **57**, 12106–12110 (2018).
47. J. Zhou *et al.*, Linking oxidative and reductive clusters to prepare crystalline porous catalysts for photocatalytic CO_2 reduction with H_2O. *Nat. Commun.* **13**, 4681 (2022).
48. H. Wang, X. Zhang, W. Zhang, M. Zhou, H. L. Jiang, Heteroatom-doped Ag(25) nanoclusters encapsulated in metal–organic frameworks for photocatalytic hydrogen production. *Angew. Chem. Int. Ed.* **63**, e202401443 (2024).
49. S. Wang *et al.*, Linker engineering of sandwich-structured metal–organic framework composites for optimized photocatalytic H_2 production. *Adv. Mater.* **35**, e2302512 (2023).
50. H. X. Liu *et al.*, Delocalized orbitals over metal clusters and organic linkers enable boosted charge transfer in metal–organic framework for overall CO_2 photoreduction. *Angew. Chem. Int. Ed.* **63**, e202411508 (2024).
51. Z. Li *et al.*, Three-component donor-π-acceptor covalent-organic frameworks for boosting photocatalytic hydrogen evolution. *J. Am. Chem. Soc.* **145**, 8364–8374 (2023).
52. Y. Li, W. Zhang, J. Niu, Y. Chen, Mechanism of photogenerated reactive oxygen species and correlation with the antibacterial properties of engineered metal-oxide nanoparticles. *ACS Nano* **6**, 5164–5173 (2012).
53. S. Yu *et al.*, Switchover from singlet oxygen to superoxide radical through a photoinduced two-step sequential energy transfer process. *Chem. Sci.* **15**, 1870–1878 (2024).
54. A. Etale, A. J. Onyianta, S. R. Turner, S. J. Eichhorn, Cellulose: A review of water interactions, applications in composites, and water treatment. *Chem. Rev.* **123**, 2016–2048 (2023).
55. K. Tu, Y. Ding, T. Keplinger, Review on design strategies and applications of metal–organic framework-cellulose composites. *Carbohydr. Polym.* **291**, 119539 (2022).
56. K. Ma *et al.*, Fibrous Zr-MOF nanozyme aerogels with macro-nanoporous structure for enhanced catalytic hydrolysis of organophosphate toxins. *Adv. Mater.* **36**, 2300951 (2023).
57. Y. H. Cheung *et al.*, Environmentally benign biosynthesis of hierarchical MOF/bacterial cellulose composite sponge for nerve agent protection. *Angew. Chem. Int. Ed.* **61**, e202202207 (2022).
58. T. Kong *et al.*, Cucumber-derived extracellular vesicle-functionalized metal–organic frameworks for enhanced photodynamic therapy of hypertrophic scars. *Adv. Funct. Mater.* **34**, 2400379 (2024).
59. Z. Zhao *et al.*, Design and synthesis of transferrable macro-sized continuous free-standing metal–organic framework films for biosensor device. *Adv. Sci.* **11**, 2310189 (2024).
60. M. Chen *et al.*, Boronic acid-decorated multivariate photosensitive metal–organic frameworks for combating multi-drug-resistant bacteria. *ACS Nano* **16**, 7732–7744 (2022).
61. L. Yan *et al.*, Metal organic frameworks for antibacterial applications. *Chem. Eng. J.* **435**, 134975–134989 (2022).
62. D. Ma *et al.*, A hydrolytically stable vanadium(IV) metal–organic framework with photocatalytic bacteriostatic activity for autonomous indoor humidity control. *Angew. Chem. Int. Ed.* **59**, 3905–3909 (2020).
63. M. Chen *et al.*, Titanium incorporation into Zr-porphyrinic metal–organic frameworks with enhanced antibacterial activity against multidrug-resistant pathogens. *Small* **16**, e1906240 (2020).
64. Y. Li, L. Liu, T. Meng, L. Wang, Z. Xie, Structural engineering of ionic MOF@COF heterointerface for exciton-boosting sunlight-driven photocatalytic filter. *ACS Nano* **17**, 2932–2942 (2023).
65. W. Guo *et al.*, Plasmon-enhanced visible-light photocatalytic antibacterial activity of metal–organic framework/gold nanocomposites. *J. Mater. Chem. A* **11**, 2391–2401 (2023).
66. Y. Chen *et al.*, Efficient Ir^{III} photosensitizer incorporated in the metal-organic framework with the bis-lophine-bipyridine motif for $C(sp^3)$-C/N–H cross-coupling reactions. *ACS Catal.* **14**, 16605–16617 (2024).
67. C. Xu, H. Liu, D. Li, J.-H. Su, H.-L. Jiang, Direct evidence of charge separation in a metal–organic framework: Efficient and selective photocatalytic oxidative coupling of amines via charge and energy transfer. *Chem. Sci.* **9**, 3152–3158 (2018).
68. X. Ding, S. Duan, X. Ding, R. Liu, F. J. Xu, Versatile antibacterial materials: An emerging arsenal for combatting bacterial pathogens. *Adv. Funct. Mater.* **28**, 1802140 (2018).
69. K. Lee *et al.*, Sunlight–activatable ROS generator for cell death using TiO_2/c-Si microwires. *Nano Lett.* **21**, 6998–7004 (2021).
70. R. Wang *et al.*, Graphdiyne-modified TiO_2 nanofibers with osteoinductive and enhanced photocatalytic antibacterial activities to prevent implant infection. *Nat. Commun.* **11**, 4465 (2020).
71. L. Wang *et al.*, An all-organic semiconductor C_3N_4/PDINH heterostructure with advanced antibacterial photocatalytic therapy activity. *Adv. Mater.* **31**, e1901965 (2019).
72. S. Ma *et al.*, Tetrathienylethene-based porous framework composites for boosting photocatalytic antibacterial activity. Cambridge Crystallographic Data Centre (CCDC). https://www.ccdc.cam.ac.uk/structures/Search?ccdc=2328617. Deposited 10 May 2024.